Integrated Behavior Simulation and Verification for a MEMS Vibratory Gyroscope Using Parametric Model Order Reduction

Honglong Chang, *Member, IEEE*, Yafei Zhang, Jianbing Xie, Zhiguang Zhou, and Weizheng Yuan

***Abstract*—In this paper, a parameterized reduced model of a vibratory microelectromechanical systems (MEMS) gyroscope is established using a parametric model order reduction algorithm. In the reduction process, not only the input angular velocity, material density, Young's modulus, and Rayleigh damping coefficient but also the coefficient of thermal expansion and the change in temperature were all preserved. Based on this model, the integrated behavior simulation of the MEMS gyroscope, including many environmental factors in engineering situations, was performed in an accurate and fast way. Compared with the finite-element method, the relative error of the reduced-order model was less than 4.2%, while the computational efficiency was improved about five times. The cosimulation with a complete interface circuit was successfully performed in a very fast way, which provides a convenient platform for designers to evaluate the performance of sensors. The experimental verification proves that the reduced model can provide a reliable simulation result, although some errors exist. [2009-0079]**

***Index Terms*—Behavior simulation, macromodel, microelectromechanical systems (MEMS), parametric model order reduction (PMOR), vibratory gyroscope.**

I. INTRODUCTION

MICROELECTROMECHANICAL systems (MEMS) are devices on a submillimeter scale. They can be an integration of sensors, actuators, and electronics on a common silicon substrate, obtained through microfabrication technology. A MEMS vibratory gyroscope is such a typical device. Thermal, electrical, and environmental actions should be accounted for in a fully coupled multiphysics modeling and simulation of the devices. A variety of modeling methods have been proposed to perform such multiphysics simulation.

The lumped-parameter (LP) method is perhaps the easiest one. By extracting LPs such as mass, damping, and stiffness, the dynamic equations or transfer functions of the MEMS devices can be established [1]–[4]. Due to the simplicity of the LP model, the complex cosimulation between the sensors and interface circuits can be carried out in a tolerable speed [5]. However, the LP model cannot reflect any geometry characteristics and does not include some parasitic mechanical modes. For MEMS gyroscope, only the driving and sensing modes can be involved.

The element network method, which decomposes the MEMS devices into a variety of lumped models like plate, beam, comb, and anchor [6]–[9], is a method frequently used in most commercial MEMS CAD software such as CoventorWare [10] and Intellisuite [11]. In such a way, the geometry and material characteristic of the microstructures can be included during modeling process. Cosimulation of the MEMS gyroscope with an interface circuit can also be performed in a fast reasonably accurate way [12], [13]. However, it would be impossible for users to add such lumped models or elements into the software suite when the available models or elements are not enough to build a new device.

The finite-element (FE) method is the most flexible and accurate solution to such a multiphysics modeling problem. Dynamic characteristics of the MEMS gyroscope [14]–[16] and impact of environment factors like thermal fluctuations [17]–[19] can be analyzed in this method. However, this method requires a high computational cost and a long simulation time. In order to insert the FE model into a circuit simulator, the behavior model can be generated from the FE simulation results [20]. However, the insertion does not preserve the physical meaning of the initial system, and some expensive full-scale physical simulations are required.

The model order reduction (MOR) method is maybe the only way to reach a balance between the speed, flexibility, and accuracy of simulation. Through this approach, the original large-dimension model can be reduced to a low-order model without much loss of accuracy. Moreover, the reduced model can be directly inserted into the system level simulators in an easy way. By now, a variety of MOR algorithms have been presented and applied. Reitz *et al.* [21] used an efficient nodal order reduction method to get the reduced model of a MEMS gyroscope from the FE model. The simulation results showed that the low-order model was accurate and efficient. Lienemann *et al.* [22] took the Arnoldi algorithm to obtain the reduced model of a Butterfly gyroscope. The simulation

Manuscript received March 26, 2009; revised October 12, 2009. First published January 19, 2010; current version published April 2, 2010. This work was supported by the Chinese Hi-Tech Research and Development Program (2007AA04Z347 and 2009AA04Z320). Subject Editor H. Seidel.

H. Chang, J. Xie, Z. Zhou, and W. Yuan are with the Micro and Nano Electromechanical Systems Laboratory, Northwestern Polytechnical University, Xi'an 710072, China (e-mail: changhl@nwpu.edu.cn; jumpingxie@163.com; zhiguang2003@163.com; yuanwz@nwpu.edu.cn).

Y. Zhang is with the Product and Engineering Simulation Laboratory, Shenzhen Institute of Advanced Technology, Chinese Academy of Sciences, Shenzhen 518055, China (e-mail: yf.zhang@sub.siat.ac.cn).

Color versions of one or more of the figures in this paper are available online at http://ieeexplore.ieee.org.

Digital Object Identifier 10.1109/JMEMS.2009.2038284

results in the time and frequency domains agreed well with those of the original model. In addition, how to preserve the passivity of the gyroscope during MOR using the Arnoldi algorithm was discussed in [23]. Gabbay *et al.* [24] used basis function methods to generate the nonlinear dynamic macromodels from 3-D physical simulations for the conservative-energy-domain behavior of electrostatically actuated devices. Mehner *et al.* [25] improved the basis function method to get the macromodel in the condition of large deflection and stress stiffening. However, the aforementioned MOR algorithms are not parameterized, which means that the MOR process would be performed again when any parameter changes. Obviously, this consequent iteration will be very time consuming.

Recently, some parametric MOR (PMOR) methods have been proposed to preserve the parameters during the MOR process [26]–[30]. They can be classified into two types. One is based on the modal superposition technique [26]. The parametric model can be extracted by the variational FE technology [31], and the geometrical parameters can be effectively preserved using the modal superposition method. The other is based on the moment matching technique. The method in [27] using the explicit moment matching technologies can cause the scale of the reduced-order model to become very large and lead to a rapid accumulation of the rounding errors. To overcome the problem, the implicit generation of the moments is often used. The mixed moments are neglected, and only pure moments are used to generate the subspace [32], [33]. Through this implicit approach, the bearing thickness and the angular velocity of a gyroscope are preserved in a reduced model [33].

In this paper, a PMOR approach based on the implicit moment matching technique is taken to generate a parametric low-order model for a typical MEMS vibratory gyroscope. In the reduction process, not only the angular velocity, material density, Young's modulus, and Rayleigh damping coefficient but also the coefficient of thermal expansion and the change in temperature are preserved. Compared with the reduced model in [33], the impact of thermal fluctuation on the performance of the gyroscope is involved into the parametric model. In addition, we found that the Coriolis matrix does not have to take part in the reduction process. Moreover, it will reduce the dimension of the macromodel dramatically due to avoiding expanding in all the parameter directions. The cosimulation with an interface circuit successfully predicted some important properties of the sensor. Comparisons with the FE method and experimental test results show that the reduced-order model can accurately and efficiently approximate the original gyroscope device when the parameters change at a certain range.

This paper is organized as follows. In Section II, we introduce the modeling object, a z-axis gyroscope, and give the vibration equation. In Section III, the algorithm to generate the parametric macromodel is described in detail. In Section IV, we verify the PMOR method by comparing the harmonic simulations with FE analysis (FEA). The cosimulation with an interface circuit of the gyroscope is successfully performed in a fast way and verified by experiments. In Section V, we discuss a few important issues about system level modeling of the gyroscope using PMOR. The conclusions are provided in Section VI.

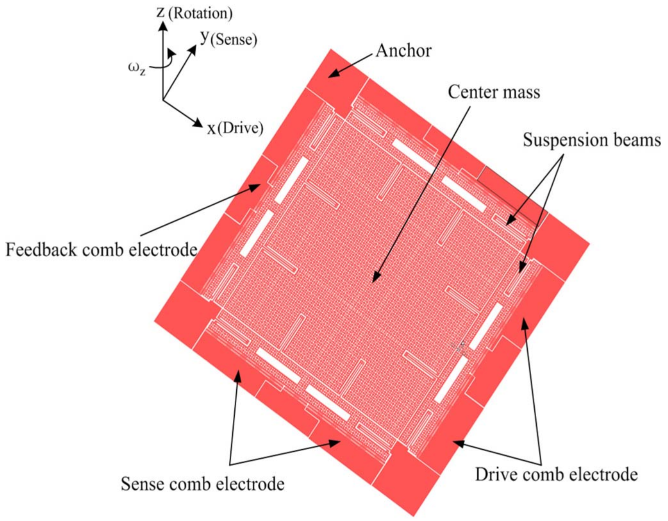

Fig. 1. Schematic of the gyroscope.

TABLE I
PARAMETERS OF THE GYROSCOPE

Parameters	Values
Young's modulus	1.3×10^{11} Pa
Poisson's ratio	0.22
Coefficient of thermal expansion	2.6×10^{-6}/°C
Temperature coefficient of Young's modulus	-7.5×10^{-5}/°C
Density	2.33×10^{3} kg/ m^3
Length of suspension beams	374×10^{-6}m
Width of suspension beams	7×10^{-6}m
Thickness of suspension beams	30×10^{-6} m
Length of center mass	1960×10^{-6} m
Width of center mass	1960×10^{-6} m
Width of comb fingers	4×10^{-6} m
Length of comb fingers	25×10^{-6}m
Gap between every two comb fingers	2×10^{-6}m
Overlap of comb finger	10×10^{-6}m
Gap between structure and substrate	7×10^{-6}m

II. MULTIPHYSICS MODELING

A. Structure and Parameters of the Gyroscope

A z-axis MEMS vibratory gyroscope with a symmetrical structure is shown in Fig. 1. The gyroscope is driven in the x-direction by an electrostatic force generated by a dc-biased ac voltage applied across the comb electrodes. The Coriolis force produced by an angular velocity input around the z-axis causes the proof mass to oscillate in the y-direction. The output signals are then detected from the capacitance change of comb electrodes in the sense direction. The various parameters of the gyroscope are shown in Table I and will be used in the following modeling and simulation process.

B. Modeling of the MEMS Gyroscope

Considering damping, temperature, electrostatic, Coriolis, and centrifugal effects simultaneously, the vibration equation with multidegrees of freedom for the MEMS vibratory gyroscope under the condition of linear elastic and small deflection,

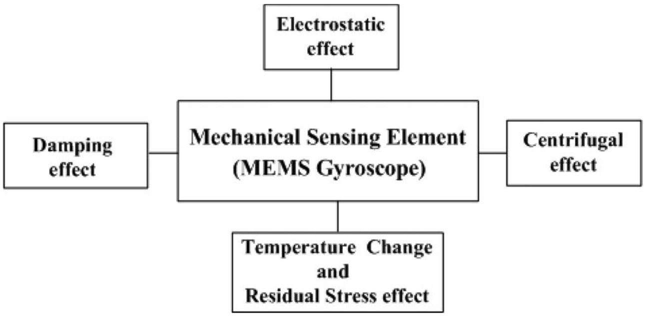

Fig. 2. Diagram of the factors involved in the vibration equation.

after discretion in space, is described by a second-order system in ordinary differential equations in time

$$\begin{aligned} &\rho\mathbf{M}\ddot{\boldsymbol{x}}(t) + (\mathbf{D} + \omega\rho\mathbf{G})\dot{\boldsymbol{x}}(t) \\ &\quad + (E\mathbf{K} + ETC_h\Delta T\mathbf{S} - \omega^2\mathbf{M}_s)\boldsymbol{x}(t) = \boldsymbol{F}_e + \boldsymbol{F}_t + \boldsymbol{F}_r \\ &\qquad\qquad\qquad\qquad\qquad \boldsymbol{y}(t) = \mathbf{L}^{\mathrm{T}}\boldsymbol{x}(t). \end{aligned} \tag{1}$$

In (1), t is the time variable, $\boldsymbol{x}(t)$ is the vector of state variables, and $\mathbf{M}$, $\mathbf{D}$, $\mathbf{G}$, $\mathbf{K}$, $\mathbf{S}$, and $\mathbf{M}_s$ are the mass, damping, Coriolis, stiffness, temperature stress-stiffening, and centrifugal mass matrices, respectively. The Coriolis matrix $\mathbf{G}$ is generated by Coriolis acceleration. $\boldsymbol{F}_e$, $\boldsymbol{F}_t$, and $\boldsymbol{F}_r$ are the electrostatic force, thermal force, and centrifugal force vectors, respectively. $\mathbf{L}$ is the output matrix, and $\boldsymbol{y}(t)$ is the output vector. The parameters ρ, ω, E, TC_h, and ΔT are the material density, input angular velocity around the z-axis, Young's modulus, the coefficient of thermal expansion, and the change in temperature, respectively.

The factors involved in the vibration equation can be depicted by a diagram as shown in Fig. 2. The damping, electrostatic, temperature, and centrifugal effects will be discussed separately in the following paragraphs.

1) Damping Effect: Viscous damping is a very important parameter in oscillating MEMS devices like vibratory gyroscopes since it mainly determines the devices' dynamic behavior. Generally, slide film damping and squeeze film damping are the two main damping effects [34]. A slide film damping occurs when two parallel plates are in relative lateral motion, whereas a squeeze film damping occurs when two parallel plates are in vertical motion.

In the gyroscope, the plates move in the $x{-}y$ plane which is parallel to the substrate. Thus, the slide film damping should be involved in the gyroscope's dynamic model. Two kinds of energy dissipative processes are shown in Fig. 3. Under the isothermal condition, the influence of the temperature on the damping behavior is not taken into account.

Couette flow assumes a constant velocity gradient across the fluid gap. Tangentially moving surfaces at low frequencies produce a nearly constant velocity gradient in the fluid, so the Couette flow is applicable to the damping at low frequencies. The damping coefficient is [35]

$$C_{\mathrm{coutte}} = \frac{\mu A}{d} \tag{2}$$

where μ is the viscosity of the fluid, A is the surface area, and d is the height of the gap.

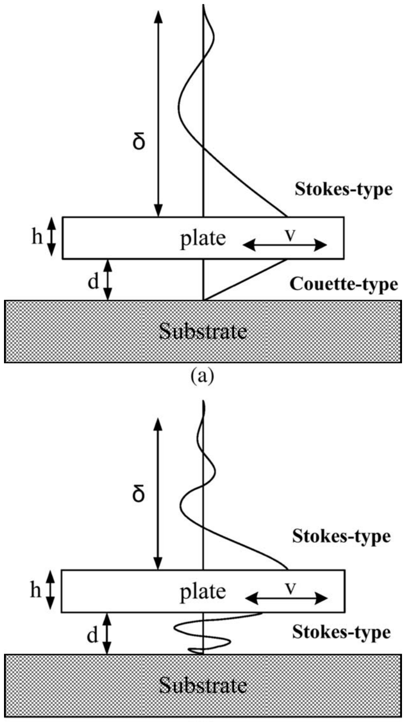

(a)

(b)

Fig. 3. Dissipative processes in the lateral moving gyroscope. (a) At low frequency. (b) At high frequency.

Stokes flow assumes that the velocity gradient is not constant across the fluid gap. Tangentially moving surfaces at high frequencies do not produce a constant velocity gradient, so the Stokes flow is applicable to the damping at high frequencies. The transition from Couette to Stokes flow occurs near the cutoff frequency f_c

$$f_c = \frac{\mu}{2\pi\rho d^2} \tag{3}$$

where ρ is the density of fluid.

The damping effects come from both the ambient fluid on the top of the moving plate and the fluid between the plates. The Stokes-type damping effect in the ambient fluid is [36]

$$C_{\mathrm{stokes}A} = \mu A\eta. \tag{4}$$

The Stokes-type damping effect underneath the plate is

$$C_{\mathrm{stokes}B} = \mu A\eta\frac{\sinh(2\eta d) + \sin(2\eta d)}{\cosh(2\eta d) - \cos(2\eta d)} \tag{5}$$

where $\eta = \sqrt{\pi f/\nu}$, with f being the oscillation frequency and ν being the kinetic viscosity.

In Fig. 3, the penetration depth δ is given by $\delta = 1/\eta$. When the operating pressure is reduced to a degree, the gas rarefaction must be included in the damping model by applying various boundary conditions such as the first-order or high-order slip boundary conditions. The behavior of the gas will change due to the gas rarefaction effect, so the effective viscosity is introduced as [35]

$$\mu_{\mathrm{eff}} = \frac{\mu}{1 + 2K_n} \tag{6}$$

where K_n is the Knudsen number which is the ratio of the mean free path λ and the gap height d

$$K_n = \frac{\lambda}{d}. \tag{7}$$

In the drive and sense modes, the coefficient of slide film damping is the sum of the damping due to both the proof mass and the comb fingers

$$c_{\text{slide}} = c_{\text{mass}} + c_{\text{combs}}. \tag{8}$$

The damping matrix $\mathbf{D}$ is often modeled as Rayleigh damping, which is a linear combination of the mass and stiffness matrices, i.e., $\mathbf{D} = \alpha \boldsymbol{M} + \beta \boldsymbol{K}$. In order to calculate the Rayleigh damping coefficients α and β, two frequencies covering the concerned modes need to be selected for further computation [37]. Herein, the frequencies of the drive mode (ω_1) and sense mode (ω_2) are chosen. The corresponding damping ratios can be obtained by

$$\begin{aligned} \xi_1 &= c_{\text{slide1}}/2\omega_1 m_1 \\ \xi_2 &= c_{\text{slide2}}/2\omega_2 m_2 \end{aligned} \tag{9}$$

where ξ_1, c_{slide1}, and m_1 are the damping ratio, damping coefficient, and the mass of the drive mode, respectively, and ξ_2, c_{slide2}, and m_2 are the damping ratio, damping coefficient, and the mass of the sense mode, respectively.

Then, the Rayleigh damping coefficient can be computed by the following equations:

$$\begin{aligned} \alpha/2\omega_1 + \beta\omega_1/2 &= \xi_1 \\ \alpha/2\omega_2 + \beta\omega_2/2 &= \xi_2 \end{aligned} \tag{10}$$

$$\begin{aligned} \alpha &= \frac{2\left(\omega_1\omega_2^2\xi_1 - \omega_1^2\omega_2\xi_2\right)}{\omega_2^2 - \omega_1^2} \\ \beta &= \frac{2\left(\omega_1\xi_1 - \omega_2\xi_2\right)}{\omega_1^2 - \omega_2^2}. \end{aligned} \tag{11}$$

2) Electrostatic Effect: The electrostatic force vector generated by a comb-drive actuator is

$$\boldsymbol{F}_e = \frac{1}{2} V(t)^2 \frac{\partial C}{\partial x} \tag{12}$$

where $V(t)$ is the driving voltage and C is the capacitance. In order to include the fringing fields of the comb fingers, the capacitance–displacement relation is computed by a series of electrostatic computations through the FE method. After least square fitting, the capacitance–displacement relation is $C = 0.00027x[\text{pF}/\mu\text{m}] + 0.00469$ [pF] as shown in Fig. 4.

The total electrostatic force can be applied on the mechanical structure by converting it to surface forces. Then, the electrostatic force vector is

$$\boldsymbol{F}_e = \frac{N}{2} V(t)^2 \frac{\partial C}{\partial x} (\mathbf{B}_{dl} + \mathbf{B}_{dr} + \mathbf{B}_{su} + \mathbf{B}_{sd}) \tag{13}$$

where N is the number of comb-drive fingers in one side of the center mass, $\mathbf{B}_{dl}$ and $\mathbf{B}_{dr}$ are the distribution matrices of the electrostatic force in the drive mode, and $\mathbf{B}_{su}$ and $\mathbf{B}_{sd}$ are the distribution matrices of the electrostatic force in the sense mode, as shown in Fig. 5.

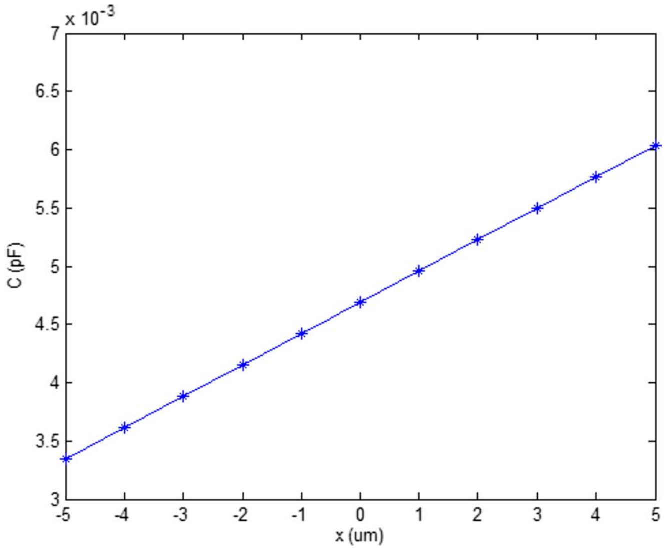

Fig. 4. Plot of capacitance–displacement relation.

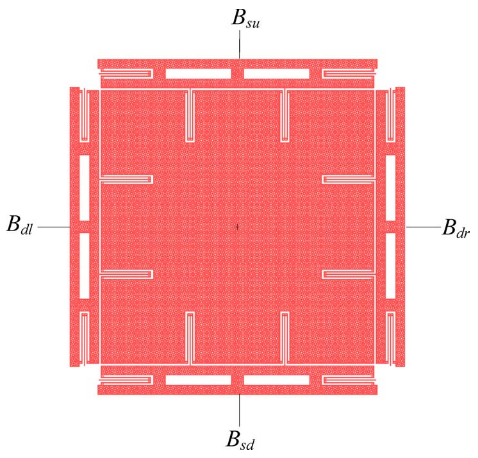

Fig. 5. Positions of the distribution matrices of the electrostatic force.

3) Thermal Fluctuation Effect: The effects of environmental thermal fluctuations on the gyroscope should be considered when estimating the actual performance of the gyroscope. The impact of temperature variation on the frequency of a system can be decomposed into three different types: changes in the modulus of the elasticity, thermal expansion, and thermally induced stress [17], [18].

The relation of Young's modulus and temperature is

$$E(T) = E(T_0) + E(T_0) TC_E \Delta T \tag{14}$$

where $E(T)$ is Young's modulus at temperature T, $E(T_0)$ is the initial value of Young's modulus, and TC_E is the temperature coefficient of Young's modulus.

The thermal load vector applied on the structure is

$$\boldsymbol{F}_t = ETC_h \Delta T \mathbf{B}_t \tag{15}$$

where $\mathbf{B}_t$ is the distribution matrix of the thermal load.

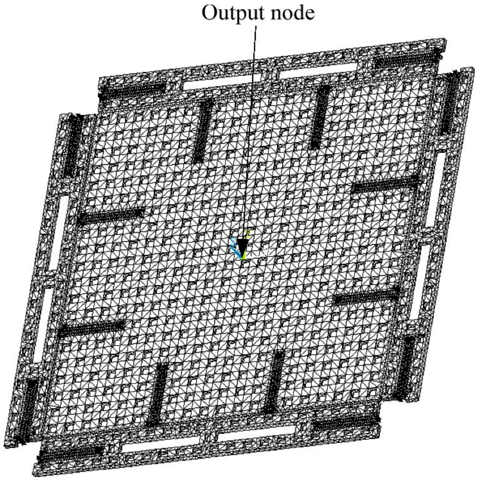

Fig. 6. FE mesh model and definition of output node.

Residual stress usually exists in many MEMS fabrication processes and has a great impact on the performance of the devices. Since the thermal stress can be calculated by $\sigma = ETC_h\Delta T$, the effect of residual stress can be modeled by a thermal load at a corresponding environment temperature.

In addition, temperature prestress effects have significant influence on the total stiffness of the structure and have therefore to be taken into account. The temperature stress-stiffening matrix $\mathbf{S}$ in the vibration equation is generated by the static thermal load, and it is a function of Young's modulus E, the coefficient of thermal expansion TC_h, and the change in temperature ΔT.

4) Centrifugal Effect: Rotation of a structure will cause a centrifugal load. The centrifugal load is

$$\boldsymbol{F}_r = \omega^2 \rho \mathbf{B}_r \tag{16}$$

where ω is the angular velocity of rotation and $\mathbf{B}_r$ is the distribution matrix of the centrifugal load.

In addition, the circumferential motions will lead to the changes in geometry of the structure. The effect can be accounted for by an adjustment of the stiffness matrix, called spin softening.

Considering the spin-softening effect, the effective stiffness matrix is

$$\overline{\mathbf{K}} = E\mathbf{K} - \omega^2 \mathbf{M}_s. \tag{17}$$

Here, a small deflection is assumed. Therefore, the change of the stiffness matrix caused by the centrifugal load is not accounted for.

C. FE Modeling

In order to extract the matrices in the vibration equation, such as $\mathbf{M}$, $\mathbf{G}$, $\mathbf{K}$, $\mathbf{S}$, $\mathbf{B}_{dl}$, $\mathbf{B}_{dr}$, $\mathbf{B}_{su}$, $\mathbf{B}_{sd}$, $\mathbf{B}_r$, and $\mathbf{L}$, the FE model of the gyroscope was constructed using the FEA tool ANSYS as shown in Fig. 6.

As the combs do not significantly impact the eigenfrequency of the structure and will obviously increase the number of nodes and result in the singular of the grids, here, the model is simplified by removing the comb fingers. In addition, the irregular holes are equivalent to square holes. It consists of 47 949 tetrahedral structural elements (SOLID187) and 110 685 nodes. Dirichlet boundary conditions are applied to all degrees of freedom of the nodes belonging to the bottom surfaces of the suspension beams, and 984 degrees of freedom are constrained. A node which is located in the center of the mass is selected as an output node for observation of the dynamic response.

III. PMOR

In order to preserve the parameters in the vibration equation, the PMOR method is used. Since the damping matrix $\mathbf{D}$ in (1) does not have to take part in the process of generation of the subspace, which has been proved by [38], it is not included in (22).

The element mass matrix is [39]

$$\mathbf{M}_e = \rho \int_V \mathbf{N}^{\mathrm{T}}\mathbf{N} \mathrm{d}v \tag{18}$$

where $\mathbf{N}$ is the element shape function matrix.

The element Coriolis matrix is

$$\mathbf{G}_e = \rho \int_V \mathbf{N}^{\mathrm{T}}\boldsymbol{\Omega}\mathbf{N} \mathrm{d}v \tag{19}$$

where $\boldsymbol{\Omega}$ is the rotational matrix. Here, only the input angular velocity around the z-axis is considered, so $\boldsymbol{\Omega}$ can be written as

$$\boldsymbol{\Omega} = \omega \begin{bmatrix} 0 & -1 & 0 \\ 1 & 0 & 0 \\ 0 & 0 & 0 \end{bmatrix}. \tag{20}$$

Therefore, the global matrices $\mathbf{M}$ and $\mathbf{G}$ can be expressed as a summation of the matrices $\mathbf{M}_e$ and $\mathbf{G}_e$ as

$$\mathbf{M} = \sum_e \mathbf{N}_e^{\mathrm{T}}\mathbf{M}_e\mathbf{N}_e \qquad \mathbf{G} = \sum_e \mathbf{N}_e^{\mathrm{T}}\mathbf{G}_e\mathbf{N}_e. \tag{21}$$

The Coriolis matrix can be obtained from the mass matrix. Therefore, in this paper, the Coriolis matrix does also take part in the process of generation of the subspace.

Then, the parameterized equation of the aforementioned gyroscope can be rewritten as

$$c_1\mathbf{M}\ddot{u}(t) + (\mathbf{K} + c_2\mathbf{S})u(t) = \frac{1}{E}(\boldsymbol{F}_e + \boldsymbol{F}_t + \boldsymbol{F}_r) \tag{22}$$

where $c_1 = \rho/E$ and $c_2 = TC_h\Delta T$.

Therefore, a total of two parameters should be accounted for during the reduction process. The stiffness matrix $\mathbf{K}$ is selected as a constant matrix to generate the projection matrix.

The Laplace transform of (14) can be written as

$$\left(c_1\mathbf{M}s^2 + (\mathbf{K} + c_2\mathbf{S})\right) X(s) = \frac{1}{E}\mathbf{B}U(s). \tag{23}$$

Then, the transfer function is

$$\begin{aligned}H(s) &= \frac{1}{E}\mathbf{L}^{\mathrm{T}}[\mathbf{K} + \tilde{s}_1\mathbf{P}_1 + \tilde{s}_2\mathbf{P}_2]^{-1}\mathbf{B}\\ &= \frac{1}{E}\mathbf{L}^{\mathrm{T}}\left[I - (-\tilde{s}_1\mathbf{K}^{-1}\mathbf{P}_1 - \tilde{s}_2\mathbf{K}^{-1}\mathbf{P}_2)\right]^{-1}\mathbf{K}^{-1}\mathbf{B}\\ &= \frac{1}{E}\mathbf{L}^{\mathrm{T}}\sum_{n=1}^{\infty}(-\tilde{s}_1\mathbf{K}^{-1}\mathbf{P}_1 - \tilde{s}_2\mathbf{K}^{-1}\mathbf{P})^n\mathbf{K}^{-1}\mathbf{B}\\ &\approx \frac{1}{E}\mathbf{L}^{\mathrm{T}}\left[\sum_{n=1}^{\infty}(-\mathbf{K}^{-1}\mathbf{P}_1)^n\mathbf{K}^{-1}\mathbf{B}\tilde{s}_1^n\right.\\ &\qquad\left.+\sum_{n=1}^{\infty}(-\mathbf{K}^{-1}\mathbf{P}_2)^n\mathbf{K}^{-1}\mathbf{B}\tilde{s}_2^n\right] \qquad (24)\end{aligned}$$

where $\tilde{s}_1 = c_1 s^2$, $\tilde{s}_2 = c_2$, $\mathbf{P}_1 = \mathbf{M}$, and $\mathbf{P}_2 = \mathbf{S}$.

Only the pure moments are computed, and the two projection matrices can be generated separately by

$$\begin{aligned}\mathrm{colspan}(\mathbf{V}_1) &= K_{r1}(-\mathbf{K}^{-1}\mathbf{P}_1, \mathbf{K}^{-1}\mathbf{B})\\ \mathrm{colspan}(\mathbf{V}_2) &= K_{r2}(-\mathbf{K}^{-1}\mathbf{P}_2, \mathbf{K}^{-1}\mathbf{B}) \qquad (25)\end{aligned}$$

where K_{r1} and K_{r2} are the Krylov subspaces of dimensions $r1$ and $r2$, respectively.

The final projection matrix $\mathbf{V}$ is composed of the aforementioned two projection matrices as

$$\mathrm{colspan}(\mathbf{V}) = \mathrm{colspan}(\mathbf{V}_1, \mathbf{V}_2). \qquad (26)$$

Then, the reduced-order system can be obtained by projecting (1) on the subspace $\mathbf{V}$

$$\begin{aligned}&\rho\mathbf{M}_r\ddot{\boldsymbol{x}}_r(t) + (\mathbf{D}_r + \omega\rho\mathbf{G}_r)\dot{\boldsymbol{x}}_r(t)\\ &\quad + (E\mathbf{K}_r + ETC_h\Delta T\mathbf{S}_r)\boldsymbol{x}_r(t) = \boldsymbol{F}_{er} + \boldsymbol{F}_{tr} + \boldsymbol{F}_{rr}\\ &\qquad\qquad \boldsymbol{y}(t) = \mathbf{L}_r^{\mathrm{T}}\boldsymbol{x}_r(t) \qquad (27)\end{aligned}$$

where

$$\begin{aligned}\mathbf{M}_r &= \mathbf{V}^{\mathrm{T}}\mathbf{M}\mathbf{V} \quad \mathbf{D}_r = \mathbf{V}^{\mathrm{T}}\mathbf{D}\mathbf{V} \quad \mathbf{G}_r = \mathbf{V}^{\mathrm{T}}\mathbf{G}\mathbf{V},\\ \mathbf{K}_r &= \mathbf{V}^{\mathrm{T}}\mathbf{K}\mathbf{V} \quad \mathbf{S}_r = \mathbf{V}^{\mathrm{T}}\mathbf{S}\mathbf{V} \quad \boldsymbol{F}_{er} = \mathbf{V}^{\mathrm{T}}\boldsymbol{F}_e,\\ \boldsymbol{F}_{tr} &= \mathbf{V}^{\mathrm{T}}\boldsymbol{F}_t \quad \boldsymbol{F}_{rr} = \mathbf{V}^{\mathrm{T}}\boldsymbol{F}_r \quad \mathbf{L}_r = \mathbf{V}^{\mathrm{T}}\mathbf{L}.\end{aligned}$$

Therefore, some important parameters such as input angular velocity, material density, Rayleigh damping coefficient, Young's modulus, the coefficient of thermal expansion, etc., are preserved because the projection matrix $\mathbf{V}$ does not depend on these parameters.

IV. SIMULATIONS AND VERIFICATIONS

By using the aforementioned PMOR algorithm, we can obtain the parameterized reduced gyroscope model. The first subspace matrix is composed of 70 vectors, and the second subspace matrix is composed of 70 vectors. The final dimension of the reduced-order model is 140. Based on this parametric reduced model, various simulations can be performed.

TABLE II
DAMPING COEFFICIENT AT DIFFERENT PRESSURE

Pressure	Damping coefficient	Rayleigh damping coefficient α	Rayleigh damping coefficient β
1 atm	1.8243×10^{-5}Ns/m	42.58/s	5.42×10^{-8}s
0.01atm	1.3794×10^{-5}Ns/m	3.22/s	4.10×10^{-9}s
0.001atm	1.0385×10^{-5}Ns/m	0.24/s	3.09×10^{-10}s

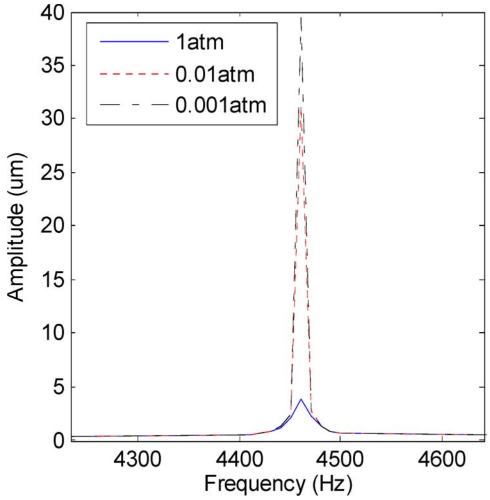

Fig. 7. Effect of damping on the gyroscope.

A. Simulations of Mechanical Part Including Multifactors

First, the damping coefficient was computed at different pressure as shown in Table II, and the amplitude of the gyroscope in the drive mode is shown in Fig. 7. It can be seen that the gyroscope can work well at atmospheric pressure. In addition, the gyroscope works at low frequency; the stiffness due to damping is neglected.

In order for comparison with the FE model, a total of 35 frequency points were evaluated between 800 Hz and 100 kHz. The harmonic response of the output node in the driving direction at atmospheric pressure is shown in Fig. 8(a). The comparison showed that the simulation results based on the original model and the reduced-order model match perfectly even at high frequency. The relative error was kept below 0.003% as shown in Fig. 8(b). The error of the harmonic response is estimated as

$$\mathrm{Error} = |H - \hat{H}|/H \qquad (28)$$

where H is the harmonic solution of the full model represented by (1) and $\hat{H}$ is the harmonic solution of the reduced-order model described by (27).

Second, the harmonic response in the sense direction at different angular velocities is shown in Fig. 9(a). It can be seen from the plot of the relative error as shown in Fig. 9(b) that the maximum error is about 0.2% when the angular velocity is 400°/s.

Finally, we got the harmonic responses at 100 °C and −60 °C as shown in Figs. 10(a) and 11(a), respectively. It showed that the frequencies also matched well due to the symmetrical structure. It is shown in Figs. 10(b) and 11(b) that the relative

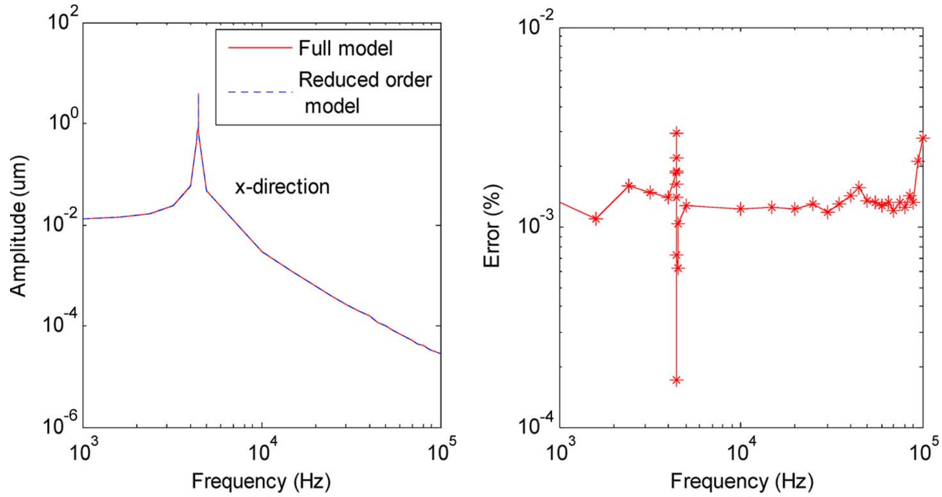

(a) (b)

Fig. 8. (a) Harmonic response in the driving direction at atmospheric pressure. (b) Error for harmonic response.

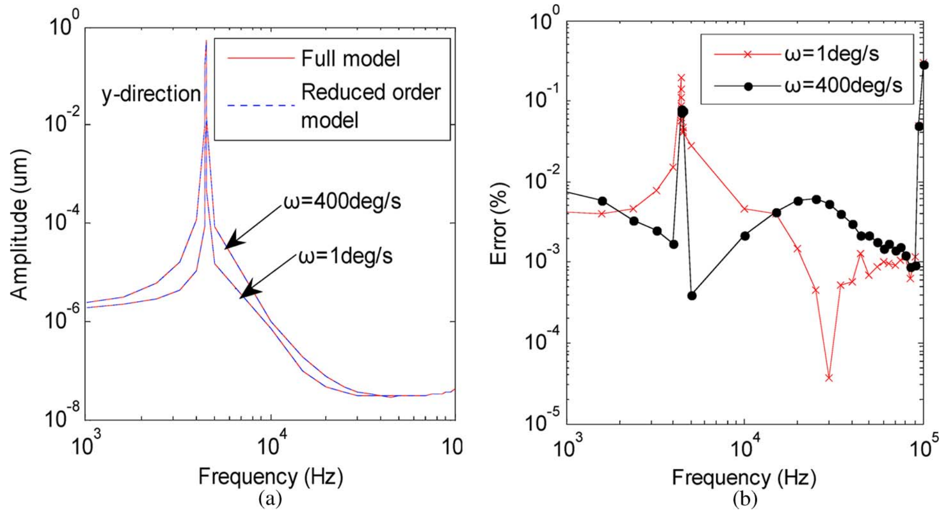

(a) (b)

Fig. 9. (a) Harmonic responses in the sensing direction at atmospheric pressure for angular velocities 1°/s and 400°/s. (b) Error for harmonic responses.

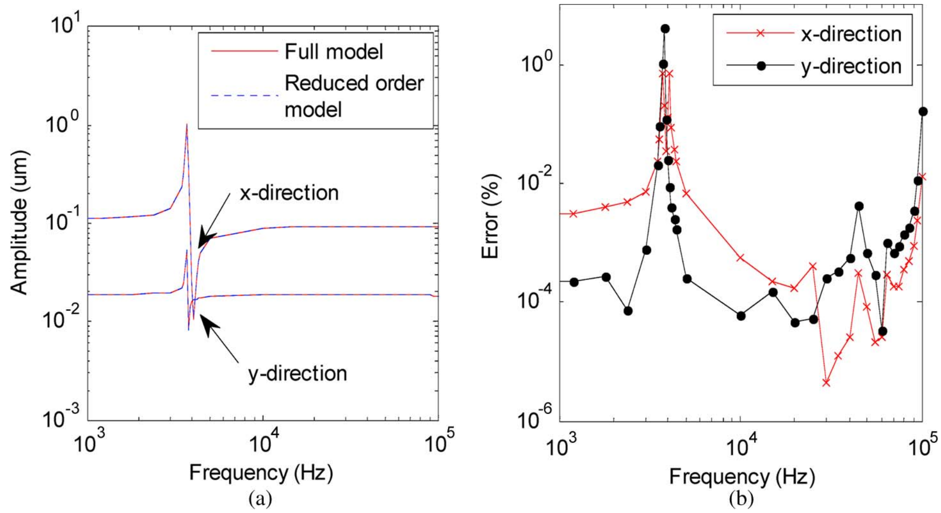

(a) (b)

Fig. 10. (a) Harmonic response at the output nodes at 100 °C. (b) Error for harmonic response.

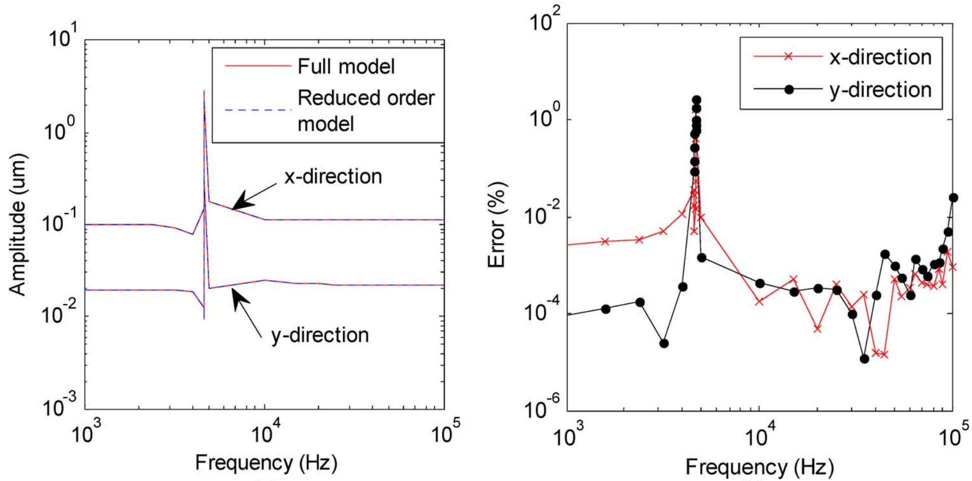

(a) (b)

Fig. 11. (a) Harmonic response at the output node at -60 °C. (b) Error for harmonic response.

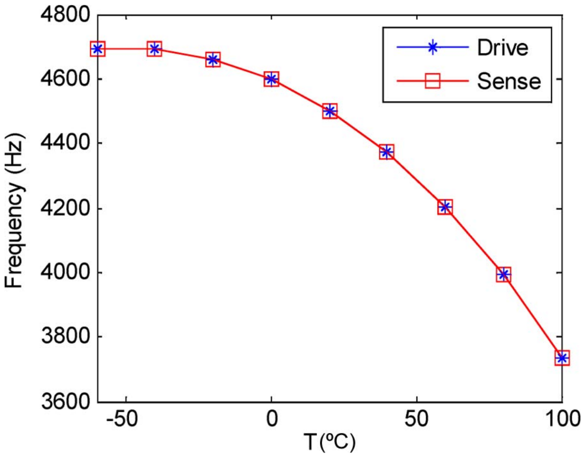

Fig. 12. Effect of thermal fluctuations on the resonant frequencies.

TABLE III
COMPARISON OF SIMULATION TIME BETWEEN THE ORIGINAL MODEL AND THE REDUCED-ORDER MODEL

Model	Size	Harmonic simulation time	Error
Original model	331071	7800s	
Reduced order model	140	1500s	4.2%

error was kept below 4.2% when the temperature changed from -60 °C to 100 °C.

The impact of thermal fluctuations on the resonant frequency was computed as shown in Fig. 12. It can be seen that the resonance frequencies of the gyroscope decrease as the temperature increases.

The computation time between the original model and the reduced-order model was compared as shown in Table III. It is obvious that the simulation speeds up five times, but the error is below 4.2%.

B. Cosimulation With Interface Circuit

The complete circuit block diagram of the gyroscope is shown in Fig. 13. The circuit consists of a self-oscillation loop and a Coriolis signal detection channel. The gyroscope resonates in the direction of the driving axis using a self-oscillation technique which is a useful method for driving a mechanical resonator at the resonant frequency. The mechanical displacement causes a change in the capacitance of the sensing electrodes. Consequently, the change in capacitance is converted to an electrical signal by a charge amplifier according to (29). The Coriolis signal is filtered, demodulated, and amplified to pick off the input angular rate signal through the Coriolis signal detection channel

$$i = V_s\left(\frac{\partial C}{\partial y}\right)\frac{dy}{dt} \qquad V = -\frac{V_s}{C_f}\left(\frac{\partial C}{\partial y}\right)y \tag{29}$$

where V_s is the amplitude of the carrier wave, C is the capacitance change of the sensing electrode, y is the displacement in the sensing direction, and C_f is the feedback capacitor of the charge amplifier.

In this simulation, the parametric reduced model and its interface circuit were described using hardware description language in Saber [40]. The frequency of the carrier wave used for modulation is 100 kHz. Accounting for the carrier signal, the time step was 1 μs, and the minimum step was 100 ns. To verify the designed interface circuit of the gyroscope in a fast way, the effect of thermal fluctuations was not temporarily considered, and the order of the reduced model was 70. When the time period was 150 ms, the total computation time was 148 000 s on a PC with 1-GB RAM and 2.30-GHz CPU.

If both the reference voltage of the automatic gain control and time constant of the low-pass filter remain unchanged, the startup time of the driving loop is 146 ms when the driving gain is 143 as shown in Fig. 14. The startup time is shortened to 19 ms when the driving gain becomes 703 as shown in Fig. 15. It can be concluded that the startup time can be reduced by increasing the driving loop gain.

The transient analysis results under a sinusoidal angular rate input are shown in Fig. 16. The five signals shown from the bottom to top are angular rate to be detected, displacement of the mass in the driving direction, displacement of the mass in the sensing direction, the electrical signal after the first

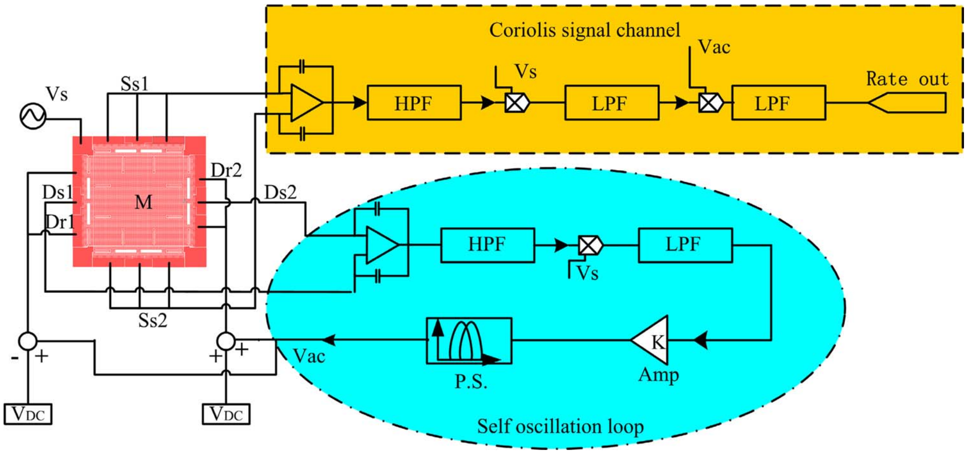

Fig. 13. Block diagram of the interface circuit for the gyroscope.

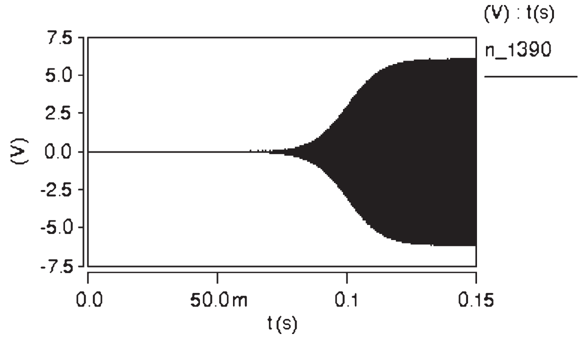

Fig. 14. Simulation result of startup time when the driving gain is 143.

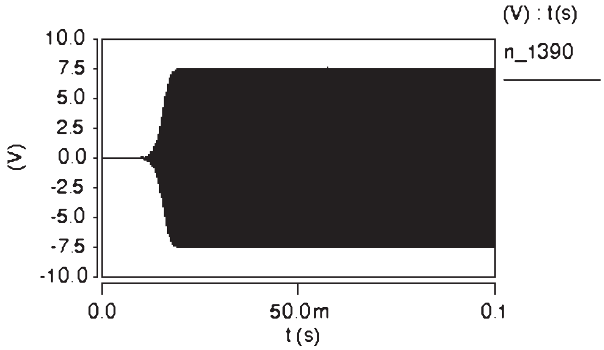

Fig. 15. Simulation result of startup time when the driving gain is 703.

demodulation, and the output signal after the second demodulation, respectively. It is obvious that the model really works well with the interface circuit.

C. Experimental Verification

In order to verify the parametric macromodel, the gyroscope was fabricated (Fig. 17) and tested in conjunction with signal conditioning electronics.

The test results of the startup time are shown in Figs. 18 and 19. From the results, it was observed that the response time is 5760 ms when the driving gain is 143, and the response time is shortened to 680 ms when the driving gain is 703. The actual startup time of the gyroscope is much longer than the simulation

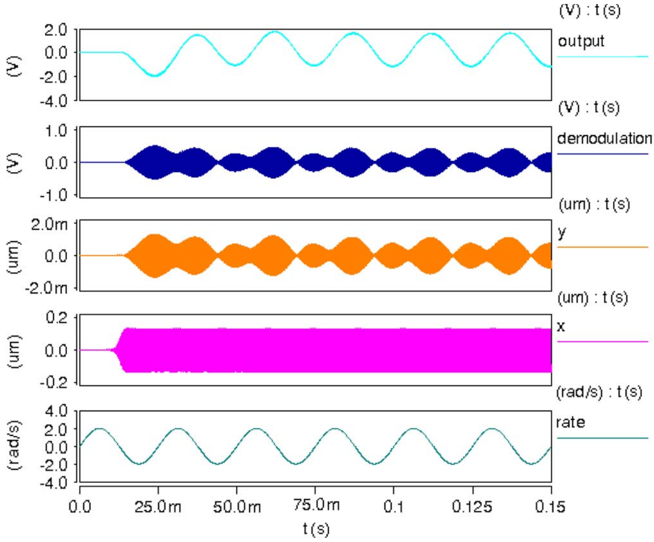

Fig. 16. Transient analysis results when the rotation rate is sine wave.

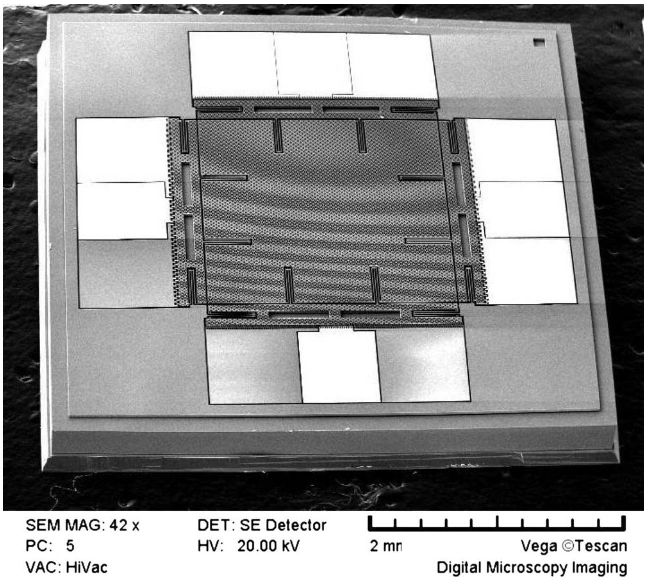

Fig. 17. SEM photograph of the gyroscope.

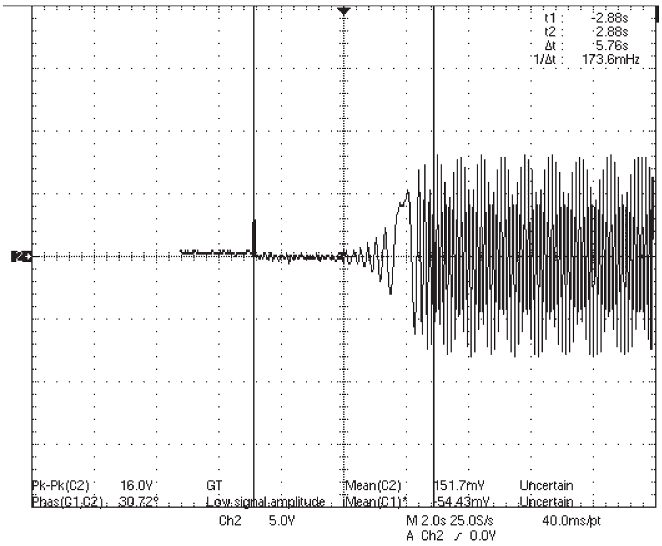

Fig. 18. Test result of startup time when the driving gain is 143.

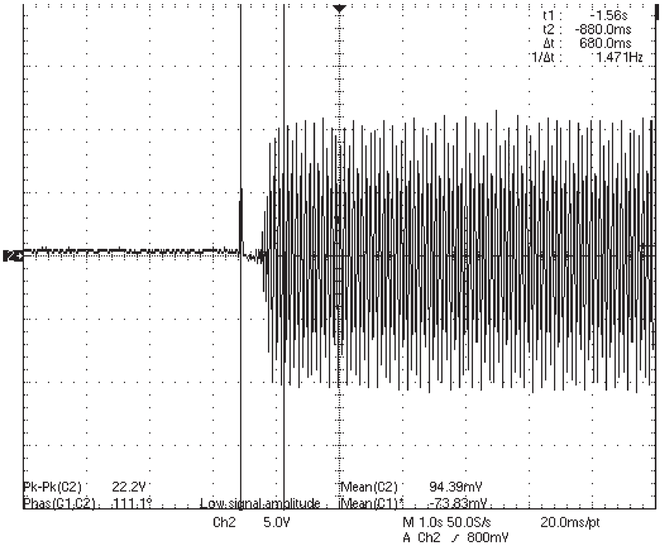

Fig. 19. Test result of startup time when the driving gain is 703.

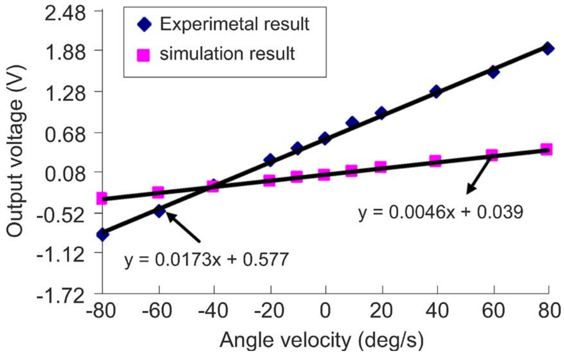

Fig. 20. Gyroscope output signal versus input angular rate.

result mainly because of the delay of the electronic devices in the experimental interface circuit.

The simulation results of the scale factor are shown and compared with the test results in Fig. 20. The experiment was carried out at room temperature and atmospheric pressure. The x-axis in the figure represents the input angular rate signal, and the y-axis represents the output voltage from the gyroscope. The square mark represents the simulation result, and the dotted line is the first-order regressive model. The value of the simulated scale factor is about 4.6 $\mathrm{mV} \cdot \mathrm{deg}^{-1} \cdot \mathrm{s}^{-1}$, which is much smaller than 17.3 $\mathrm{mV} \cdot \mathrm{deg}^{-1} \cdot \mathrm{s}^{-1}$ of the test result with a diamond mark.

Through the aforementioned comparisons with the FE method and experimental test results, we could find that the parametric macromodel fits very well with the FE model with a much better simulation efficiency, while big errors occur when compared with the experimental test results. It is obvious that the errors are caused by the big differences between the ideal model and the realities. Sometimes, the difference is really hard to measure and be incorporated into the model. Anyway, the parametric macromodel-based simulation shows an accordant and reliable prediction through the experimental verification, which provides a useful design tool for the evaluation of the sensors' performance.

V. DISCUSSION

In previous sections, we have demonstrated that the PMOR method for a MEMS vibratory gyroscope can really reduce the dimensions of the full model considerably and preserve those important parameters and the accuracy simultaneously. In this section, we will discuss a few important issues about system level modeling of the microgyroscope using PMOR.

Different from the traditional MOR method, PMOR needs Taylor expansion in different parameter directions. During the process, there will be a large number of mixed moments. The number of mixed moments grows linearly as the iteration goes on. If many parameters need to be preserved, it usually leads to a high-dimensional system and a rapid accumulation of the rounding errors. Thus, we can neglect the mixed moments and perform separated Taylor expansions in all the parameter directions. Then, the number of moments can be selected according to their importance. However, the order of the reduced model is very high if considering many parameters. Therefore, keeping the accuracy within a certain range makes the order of the macromodel lower, which is better. Eid *et al.* have proven that the Rayleigh damping matrix is unnecessary to be taken into account for generation of the subspace. Here, we find that the Coriolis matrix neither has to take part in the reduction. Moreover, it will reduce the dimension of the macromodel dramatically due to avoiding expanding in all the parameter directions.

When cosimulating with the interface circuit, the frequency of the carrier wave in the interface circuit is usually larger than 100 kHz, and the generated macromodel must consider properties at high frequency. In order to ensure the accuracy of the macromodel at high frequency, more moments need to be generated along the frequency direction, which will lead to a larger dimensional system. On the other hand, the typical resonant frequency of the MEMS inertial sensors is about 1–20 kHz. The different time scales of the mechanical structure and the circuit cause the cosimulation to become very time consuming and hard to be convergent. To speed up the simulation, the order of the macromodel should be as low as possible. Thus, the tradeoffs must be made to determine the order of the reduced model.

VI. CONCLUSION

Through the aforementioned experiments and discussions, we can draw some conclusions.

First, the PMOR method is the most efficient way to enable the integrated behavior simulation in an accurate and fast way. It can get a faster simulation speed than the FE method and a better accuracy than the LP method. In this paper, the simulation of the gyroscope based on PMOR kept the relative error within 4.2%, while the computational efficiency improved about five times compared with the FE method.

Second, the PMOR algorithm can be applied to not only the components such as damping in perforated plates and folded beams but also to a complex system like a gyroscope. In this paper, a vibratory MEMS gyroscope has been successfully reduced in a parametric way. In addition, we have found that, during reduction, the expansion in the angular velocity direction is unnecessary.

Finally, the integrated behavior simulation based on the parametric macromodel provides a good design platform for MEMS devices such as gyroscope and accelerometer. Various design tasks such as circuit design and performance evaluation can be finished in this platform.

ACKNOWLEDGMENT

The authors would like to thank Prof. E. Rudnyi for his help with the matrix extraction and the IMTEK at Freiburg University for the tools-mor4ansys.

REFERENCES

[1] S. Rajendran and K. M. Liew, "Design and simulation of an angular-rate vibrating microgyroscope," *Sens. Actuators A, Phys.*, vol. 116, no. 2, pp. 241–256, Oct. 2004.

[2] S. Mohite, N. Patil, and R. Pratap, "Design, modeling and simulation of vibratory micromachined gyroscopes," *J. Phys., Conf. Ser.*, vol. 34, pp. 757–763, 2006.

[3] A. Ongkodjojo and F. E. H. Tay, "Global optimization and design for microelectromechanical systems devices based on simulated annealing," *J. Micromech. Microeng.*, vol. 12, no. 6, pp. 878–897, Nov. 2002.

[4] W. Z. Yuan, X. L. Lv, and W. J. Li, "Multiple-domain coupling analysis based on lumped parameter macromodel for micromachined gyroscope," *China Mech. Eng.*, vol. 17, pp. 401–405, Feb. 2006.

[5] A. Lee, H. Ko, Y. Park, K. Yoo, S. W. Kim, S. C. Lee, J.-S. Lim, T. Ahn, D.-K. Jeong, H.-S. Jang, M. H. Park, and D. Cho, "Modeling and simulation of the microgyroscope driving loop using SPICE," *J. Phys., Conf. Ser.*, vol. 34, pp. 1020–1025, 2006.

[6] G. Lorenz, R. Neul, and B. G. Robert, "Network-type modeling of micromachined sensors system," in *Proc. Int. Conf. Modeling Simul. Microsyst.*, Santa Clara, CA, 1998, pp. 233–238.

[7] G. K. Fedder and Q. Jing, "A hierarchical circuit-level design methodology for microelectromechanical systems," *IEEE Trans. Circuits Syst. II, Analog Digit. Signal Process.*, vol. 46, no. 10, pp. 1309–1315, Oct. 1999.

[8] T. Mukherjee and G. K. Fedder, "Hierarchical mixed-domain circuit simulation, synthesis and extraction methodology for MEMS," *J. VLSI Signal Process.*, vol. 21, no. 3, pp. 233–249, Jul. 1999.

[9] J. V. Clark, N. Zhou, and K. S. J. Pister, "MEMS simulation using SUGAR v0.5," in *Proc. Solid-State Sens. Actuators Workshop*, Hilton Head Island, SC, 1998, pp. 191–196.

[10] CoventorWare, San Mateo, CA. [Online]. Available: http://www.coventor.com

[11] IntelliSuite, Woburn, MA: IntelliSense Corp. [Online]. Available: http://www.intellisense.com

[12] J. E. Vandemeer, "Nodal design of actuators and sensors (NODAS)," M.S. thesis, Dept. Elect. Comput. Eng., Carnegie Mellon Univ., Pittsburgh, PA, May, 1998.

[13] M. Kranz, "Design, simulation, and implementation of two novel micromechanical vibratory-rate gyroscopes," M.S. thesis, Dept. Elect. Comput. Eng., Carnegie Mellon Univ., Pittsburgh, PA, May 1998.

[14] Y. L. Zhu, S. H. R. Wang, and A. P. Qiu, "Finite element analysis of the micromechanical resonant gyroscope," *J. Southeast Univ.-Natural Science Edition*, vol. 34, no. 1, pp. 38–41, Jan. 2004.

[15] J. S. Han and B. M. Kwak, "Robust optimal design of a vibratory microgyroscope considering fabrication errors," *J. Micromech. Microeng.*, vol. 11, no. 6, pp. 662–671, Nov. 2001.

[16] B. Lv, X. Liu, Z. Yang, and G. Yan, "Simulation of a novel lateral axis micromachined gyroscope in the presence of fabrication imperfections," *Microsyst. Technol.*, vol. 14, no. 6, pp. 711–718, Jun. 2008.

[17] C. C. Painter and A. M. Shkel, "Structural and thermal modeling of a z-axis rate integrating gyroscope," *J. Micromech. Microeng.*, vol. 13, no. 2, pp. 229–237, Mar. 2003.

[18] C. C. Painter and A. M. Shkel, "Structural and thermal analysis of a MEMS angular gyroscope," *Proc. SPIE*, vol. 4334, pp. 86–94, 2001.

[19] G. Liu, A. Wang, T. Jiang, J. Jiao, and J. B. Jang, "Effects of environmental temperature on the performance of a micromachined gyroscope," *Microsyst. Technol.*, vol. 14, no. 2, pp. 199–204, Apr. 2008.

[20] Y. Ansel, P. Lerch, P. Renaud, and F. Paoletti, "Simulation and design of three axis navigation microsystem based on micromachined sensors," in *Proc. Simul. Des. Microsyst. Microstruct.*, 1997, pp. 107–116.

[21] S. Reitz, J. Bastian, J. Haase, P. Schneider, and P. Schwarz, "System level modeling of the relevant physical effects of inertial sensors using order reduction methods," *Analog Integr. Circuits Signal Process.*, vol. 37, pp. 7–16, Jul. 2005.

[22] J. Lienemann, D. Billger, E. B. Rudnyi, A. Greiner, and J. G. Korvink, "MEMS compact modeling meets model order reduction: Examples of the application of Arnoldi methods to microsystem devices," in *Proc. NANOTECH Conf.*, 2004, pp. 303–306.

[23] R. Zhang, W. Wang, A. Dounavis, and G. A. Jullien, "Passive reduced-order macromodeling algorithm for microelectromechanical systems," *J. Microelectromech. Syst.*, vol. 17, no. 3, pp. 678–687, Jun. 2008.

[24] L. D. Gabbay, J. E. Mehner, and S. D. Senturia, "Computer-aided generation of reduced-order dynamic macromodels—I: Geometrically linear motion," *J. Microelectromech. Syst.*, vol. 9, no. 2, pp. 262–269, Jun. 2000.

[25] J. E. Mehner, L. D. Gabbay, and S. D. Senturia, "Computer-aided generation of nonlinear reduced-order dynamic macromodels—II: Stress-stiffened motion," *J. Microelectromech. Syst.*, vol. 9, no. 2, pp. 270–278, Jun. 2000.

[26] V. Kolchuzhin, W. Dotzel, and J. Mehner, "A derivatives based method for parameterization of MEMS reduced order models," in *Proc. 9th Int. Conf. Therm., Mech. Multiphysics Simul. Experiments Micro-Electron. Micro-Syst., EuroSimE*, Freiburg-im-Breisgau, Germany, Apr. 21–23, 2008, pp. 519–523.

[27] L. Daniel, O. C. Siong, L. S. Chay, K. H. Lee, and J. White, "A multiparameter moment-matching model- reduction approach for generating geometrically parameterized interconnect performance models," *IEEE Trans. Comput.-Aided Design Integr. Circuits Syst.*, vol. 23, no. 5, pp. 678–693, May 2004.

[28] L. H. Feng, E. B. Rudnyi, and J. G. Korvink, "Preserving the film coefficient as a parameter in the compact thermal model for fast electrothermal simulation," *IEEE Trans. Comput.-Aided Design Integr. Circuits Syst.*, vol. 24, no. 12, pp. 1838–1847, Dec. 2005.

[29] C. Moosmann, E. B. Rudnyi, A. Greiner, J. G. Korvink, and M. Hornung, "Parameter preserving model order reduction of a flow meter," in *Proc. Nanotech*, 2005, vol. 3, pp. 684–687.

[30] L. H. Feng, D. Koziol, E. B. Rudnyi, and J. G. Korvink, "Parametric model reduction for fast simulation of cyclic voltammograms," *Sens. Lett.*, vol. 4, no. 2, pp. 165–173, Apr. 2006.

[31] J. E. Mehner, A. Schaporin, V. Kolchuzhin, W. Doetzel, and T. Gessner, "Parametric model extraction for MEMS based on variational finite element techniques," in *Proc. 13th Int. Conf. Solid-State Sens., Actuators, Microsyst.*, Seoul, Korea, Jun. 2005, pp. 776–779.

[32] E. B. Rudnyi, L. H. Feng, M. Salleras, S. Marco, and J. G. Korvink, "Error indicator to automatically generate dynamic compact parametric thermal models," in *Proc. Therminic*, Sep. 2005, pp. 139–145.

[33] C. Moosmann, "ParaMOR—Model Order Reduction for parameterized MEMS applications," M.S. thesis, Dept. Microsyst. Eng., Freiburg Univ., Freiburg, Germany, 2007.

[34] S. D. Senturia, *Microsystem Design*. Boston, MA: Kluwer, 2001.

[35] T. Veijola and M. Turowski, “Compact damping models for laterally moving microstructures with gas-rarefaction effects,” *J. Microelectromech. Syst.*, vol. 10, no. 2, pp. 263–273, Jun. 2001.
[36] Y. H. Cho, A. P. Pisano, and R. T. Howe, “Viscous damping model for laterally oscillating microstructures,” *J. Microelectromech. Syst.*, vol. 3, no. 2, pp. 81–87, Jun. 1994.
[37] I. Chowdhury and S. P. Dasgupta, “Computation of Rayleigh damping coefficients for large systems,” *Electron. J. Geotech. Eng.*, vol. 8, 2003, Bundle 8C. [Online]. Available: http://www.ejge.com/2003/Ppr0318/Ppr0318.pdf
[38] R. Eid, B. Salimbahrami, B. Lohmann, E. B. Rudnyi, and J. G. Korvink, “Parametric order reduction of proportionally damped second-order systems,” *Sens. Mater.*, vol. 19, no. 3, pp. 149–164, Oct. 2006.
[39] D. Guo and F. L. Chu, “The influence of rotation on vibration of a thick cylindrical shell,” *J. Sound Vib.*, vol. 242, no. 3, pp. 487–505, May 2001.
[40] Saber Accelerates Robust Design, Manage Mechatronic Complexity, 2009. [Online]. Available: http://www.synopsys.com/Tools/SLD/Mechatronics/Saber/Pages/default.aspx

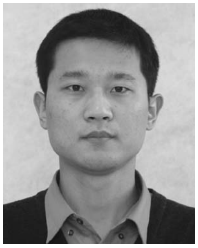

Honglong Chang (M’04) received the B.S., M.S., and Ph.D. degrees in mechanical engineering from Northwestern Polytechnical University (NPU), Xi’an, China, in 1999, 2002, and 2005, respectively.

Since April 2007, he has been an Associate Professor in the Micro and Nano Electromechanical Systems Laboratory, NPU. His current principal research activities are the development of CAD systems for design and simulation of MEMS devices.

Dr. Chang is a Reviewer for the IEEE/ASME TRANSACTIONS ON MECHATRONICS.

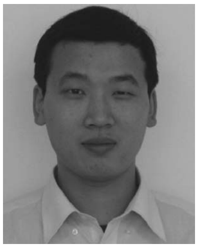

Yafei Zhang received the B.S. degree in mechanical engineering from Hebei University of Science and Technology, Shijiazhuang, China, in 2006, and the M.S. degree from Northwestern Polytechnical University, Xi’an, China, in 2009.

He is currently a Research Assistant in the Product and Engineering Simulation Laboratory, Shenzhen Institute of Advanced Technology, Chinese Academy of Sciences, Shenzhen, China. His research focuses on reduced-order modeling and engineering simulation.

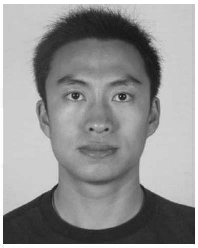

Jianbing Xie received the M.S. degree in mechanical engineering from Northwestern Polytechnical University, Xi’an, China, in 2006, where he is currently working toward the Ph.D. degree.

His research focuses on microfabrication technology.

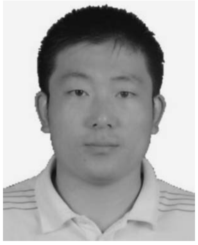

Zhiguang Zhou received the B.S. degree in electrical engineering from Northwestern Polytechnical University, Xi’an, China, in 2007, where he is currently working toward the M.S. degree and works on microgyroscope electronics.

Weizheng Yuan received the Ph.D. degree in mechanical engineering from Northwestern Polytechnical University (NPU), Xi’an, China, in 1996.

He is currently the Director of the Micro and Nano Electromechanical Systems Laboratory, NPU. His research interests include microsensors, microoptics, and applications of microelectromechanical systems.